

Controlling Orientational and Translational Order of Iron Oxide Nanocubes by Assembly in Nanofluidic Containers

Michael Agthe,[†] Kristin Høydalsvik,^{‡,§} Arnaud Mayence,[†] Petri Karvinen,^{||,⊥} Marianne Liebi,[#] Lennart Bergström,^{*,†} and Kim Nygård^{*,‡}

[†]Department of Materials and Environmental Chemistry, Stockholm University, SE-10691 Stockholm, Sweden

[‡]Department of Chemistry and Molecular Biology, University of Gothenburg, SE-41296 Gothenburg, Sweden

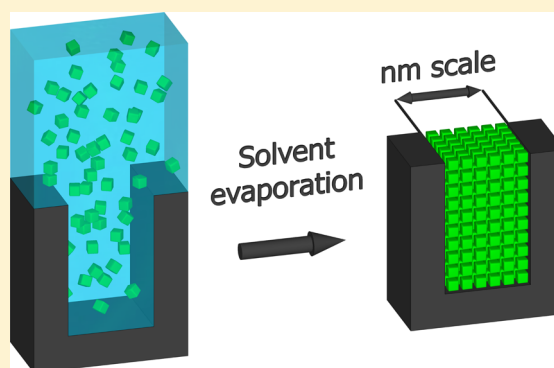
[§]Department of Materials Science and Engineering, Norwegian University of Science and Technology, NO-7491 Trondheim, Norway

^{||}Institute of Photonics, University of Eastern Finland, FI-80100 Joensuu, Finland

[⊥]Finnlitho Ltd, FI-80140 Joensuu, Finland

[#]Paul Scherrer Institut, CH-5232 Villigen PSI, Switzerland

ABSTRACT: We demonstrate that spatial confinement can be used to control the orientational and translational order of cubic nanoparticles. For this purpose we have combined X-ray scattering and scanning electron microscopy to study the ordering of iron oxide nanocubes that have self-assembled from toluene-based dispersions in nanofluidic channels. An analysis of scattering vector components with directions parallel and perpendicular to the slit walls shows that the confining walls induce a preferential parallel alignment of the nanocube (100) faces. Moreover, slit wall separations that are commensurate with an integer multiple of the edge length of the oleic acid-capped nanocubes result in a more pronounced translational order of the self-assembled arrays compared to incommensurate confinement. These results show that the confined assembly of anisotropic nanocrystals is a promising route to nanoscale devices with tunable anisotropic properties.



INTRODUCTION

The self-assembly of nanoparticles (NPs) into ordered structures is a promising strategy for the production and design of nanostructured materials with novel properties. Previous work has shown that ordered arrays of NPs combine the properties of the nanocrystalline building blocks with the collective properties of the interacting NPs in the ordered structure.^{1–3} This is essential as the collective properties and organization of interacting nano-objects are key to the final performance. While the assembly of nanospheres into densely packed arrays with defined structures is well-established,^{4,5} nonspherical NPs are attracting rapidly growing interest due to the possibility of tuning the electronic, optical, and magnetic properties by controlling both the size and shape.^{6,7} However, the development of tunable and robust methods for assembling nonspherical NPs into periodically packed structures is a challenge.^{8,9} The structure of the mesoscale assemblies has been controlled by using light or external electrical or magnetic fields to tune the magnitude and directionality of the interparticle forces.^{10–12} The topography of the substrate^{13–15} and directional particle attachment^{16,17} have also been shown to have a profound effect on the resulting structures.

A conceptually simple and appealing approach for controlling the mesoscale assembly of NPs is by means of spatial confinement. In essence, the confining solid walls impose

packing constraints on the particles, thus leading to their enhanced mesoscale order.¹⁸ Moreover, the resulting structures can be controlled by the confinement geometry; more pronounced ordering is expected when the confining wall separation W is commensurate with the particle size, i.e., when an integer multiple of the particle size barely fits in the confining slit, while less pronounced order is observed for incommensurate confinement. However, while mesoscale ordering of block copolymers^{19,20} and spherical particles^{21–23} in confinement has been addressed before, studies on confinement-induced ordering of nonspherical NPs are scarce.

A major challenge in studies on confinement-induced mesoscale NP assembly is the presence of confining walls, which hampers experimental characterization. Consequently, mature experimental techniques, such as grazing-incidence small-angle X-ray scattering (GISAXS),^{24–27} become highly challenging. We have recently developed an experimental scheme to resolve this problem²⁸ by confining NP dispersions in specifically designed nanofluidic containers and employing small-angle X-ray scattering (SAXS) in transmission mode for

Received: October 2, 2015

Revised: October 28, 2015

Published: October 28, 2015

structural characterization. Here we apply this unique approach to probe the assembly of magnetite nanocubes in confinement.

In this study we address the mesoscale order of spatially confined cubic NPs by drop-casting a concentrated dispersion of iron oxide nanocubes in toluene into nanofluidic containers. Next we probe the structural order at both mesoscopic and atomic length scales using simultaneous SAXS and wide-angle X-ray scattering (WAXS), averaged over a thousand confining channels. For a schematic of the experiment and geometric definitions we refer to Figure 1. Finally, we verify the mesoscale

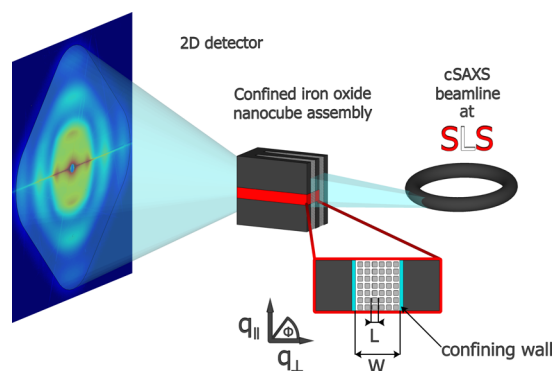


Figure 1. Schematic of the X-ray scattering experiment. The incident X-rays impinge parallel to the confining walls, and SAXS/WAXS data are collected in transmission mode as a function of scattering vector components parallel (q_{\parallel}) and perpendicular (q_{\perp}) to the confining walls. The separation between the confining walls is denoted by W , and the average NP edge length by L .

order in real space using scanning electron microscopy (SEM) on cross sections of cleaved NP-filled channel arrays. Thereby we demonstrate that mesoscale order of the magnetite nanocubes is induced by the confining walls and that the nanocubes align one of their faces, and hence the corresponding $\{100\}$ planes, parallel to the confining slit walls.

EXPERIMENTAL SECTION

Synthesis of Magnetite Nanocubes. The synthesis and purification of iron oxide nanocubes with a narrow size distribution has been described in a recent paper.²⁹ In brief, a 10 mmol iron oleate precursor was dispersed in 50 mL of 1-octadecene (Sigma-Aldrich) and 2.56 g of eicosane (Sigma-Aldrich) and mixed with 5 mmol each of sodium oleate (97%, TCI) and oleic acid (99%, TCI). The thermal decomposition of the precursor starts with degassing the solution at 120 °C for 20 min, heating until 325 °C at 3 °C/min, and keeping the mixture at 325 °C for 30 min, followed by rapid cooling to room temperature. After centrifuging the mother liquor several times with a solvent–nonsolvent mixture (toluene–ethanol), an almost dry powder indicates the removal of most synthesis organics. A storable, redispersible paste is obtained by adding oleic acid (0.05 mg of oleic acid per mg of paste) and homogenizing the toluene-dispersed nanocubes with ultrasound. For improved size distribution a centrifugation step discarding aggregates from the purification process was employed. Finally, the paste is produced by gently drying the centrifuged supernatant under vacuum and storing under nitrogen.

The resulting oleic acid-coated cubic NPs consist of magnetite, a mixed-oxide inverse spinel structure of Fe_2O_3 and FeO with space group $Fd\bar{3}m$. X-ray diffraction (XRD, Figure 2) showed the lattice constant of the NPs to be $a = 0.8370$ nm, slightly smaller than the nominal value of $a = 0.8397$ nm for magnetite. Such a minor decrease of the lattice constant has been observed previously for cubic magnetite NPs.³⁰

Manufacturing of Nanofluidic Containers. The nanofluidic containers were manufactured using electron beam lithography (Raith

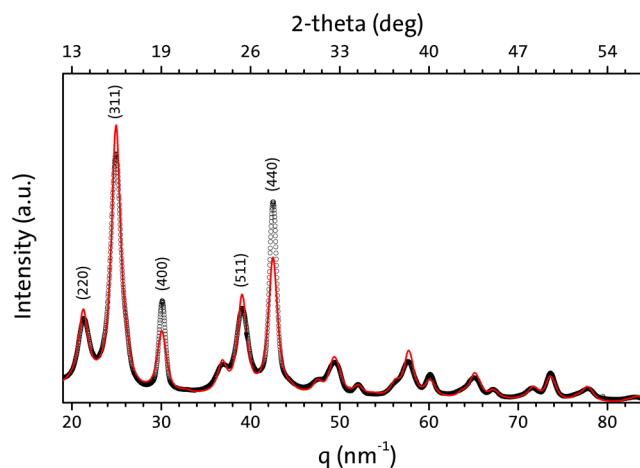


Figure 2. XRD pattern obtained from the cubic magnetite NPs. The red curve denotes a Rietveld refinement, providing lattice parameter $a = 0.8370$ nm. We attribute the deviations in intensity between experimental data and refinement to texture.

EBPG5000 Plus) and reactive ion etching (RIE, Oxford Instruments PL100). First a mask was fabricated on a standard silicon wafer using a negative-tone hydrogen silsesquioxane (HSQ) resist applying an area dose of 5000 $\mu\text{C}/\text{cm}^2$ with an acceleration voltage of 100 kV. All exposure parameters except the exposed line width were kept constant for nanofluidic containers with different widths. Afterward the RIE was conducted using hydrogen bromide (HBr) and oxygen-based chemistry and inductively coupled plasma (ICP). The etching gas ratio was 20:1 for HBr/oxygen; the etching was conducted under a pressure of 2.5 mTorr using rf power and ICP power of 120 and 700 W, respectively. These parameters resulted in an etching speed of 110 nm/min, although one has to remember that these values depend heavily on the equipment used. The remaining HSQ mask was removed using buffered hydrofluoric acid.

Small- and Wide-Angle X-ray Scattering. We carried out the combined SAXS and WAXS experiment at the cSAXS instrument of the Swiss Light Source, Paul Scherrer Institut, Switzerland. We used an incident X-ray wavelength of $\lambda = 0.100$ nm and a beam size at the sample of approximately 0.2×0.2 mm². The incident X-rays impinged parallel to the confining surfaces and were focused onto the detector plane in order to maximize the resolution. We collected simultaneous SAXS and WAXS data in transmission geometry by mounting single-photon-counting PILATUS 2M and 300k detectors³¹ 2.2 and 0.65 m behind the sample, respectively. Finally, we placed an evacuated flight tube between the sample and the detectors in order to minimize parasitic scattering.

Transmission Electron Microscopy. High-resolution transmission electron microscopy (TEM) and electron diffraction were acquired using a JEOL JEM-2100F (JEOL, Japan, Schottky-type FEG, point resolution = 0.19 nm, operated at 200 kV).

NP size determination by TEM was carried out on a JEOL JEM-2100 (JEOL, Japan, LaB₆ filament operated at 200 kV) equipped with a Gatan Orius SC 1000 camera. The size distribution of the nanocubes was determined by semiautomatic image analysis of 4324 particles with software package ImageJ (v. 1.49). Ill-segmented particles as well as particles at the image edges were removed from the analysis. Image calibration was achieved by comparing lattice spacing d_{220} or d_{400} of selected particles with the known lattice constant of the inverse spinel structure of magnetite from XRD characterization.

Scanning Electron Microscopy. We performed SEM imaging of both empty and NP-filled nanofluidic containers. Access into the different gratings was achieved by cleaving the silicon substrate perpendicular to the gratings' long axis. In the former case we made use of an LEO 1550 Gemini microscope (5 kV, WD: 9.2 mm), while in the latter case we used an FEI Magellan 400 extreme high-resolution

microscope (FEI, USA, 1 nm resolution at 3 kV, beam current 6.3 pA, WD 4 mm) using the through-lens detector in immersion mode.

X-ray Diffraction. XRD characterization was performed on dried nanocube paste placed on top of a thin glass capillary. Diffraction images were acquired on an Xcalibur-III single-crystal X-ray diffractometer (Oxford Instruments, United Kingdom) using Mo $K\alpha$ radiation ($\lambda_{K\alpha 1} = 0.07093$ nm) and a beam size of 500 μm . The Sapphire 3 CCD area detector was rotated around the sample at a distance of 100 mm and in a 2θ range of 0 to 80° in steps of 10° with an acquisition time of 500 s for each image. Software package MAUD v. 2.53³² was used for Rietveld refinement of the integrated diffraction patterns.

RESULTS AND DISCUSSION

Magnetite Nanocubes and Drop-Casting. Throughout this study we make use of cubic iron oxide NPs, as shown in the TEM images of Figure 3. The nanocubes have an average edge

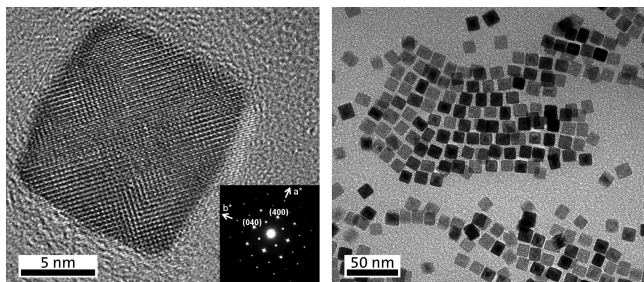


Figure 3. TEM images of the iron oxide NPs, demonstrating their nearly cubic shape. The inset in the left panel shows an electron diffraction pattern of the nanocube recorded along the [001] zone axis. The diffraction pattern is consistent with the magnetite/maghemite phase, and no other phase is observed.

length of $L_{\text{edge}} = (12.4 \pm 1.0)$ nm with a standard deviation of $\sigma = 1.0$ nm, as determined by TEM in Figure 4. Taking into account the ca. 1.9-nm-thick stabilizing oleic acid layer, we obtain an average total edge length of $L = (16.2 \pm 1.0)$ nm.

In order to verify the size of the nanocubes, we collected SAXS data from a dilute bulk dispersion (0.08 vol % of NPs) of the cubic magnetite NPs dispersed in toluene. From the small-angle (low- q) limit of these SAXS data we obtain the radius of

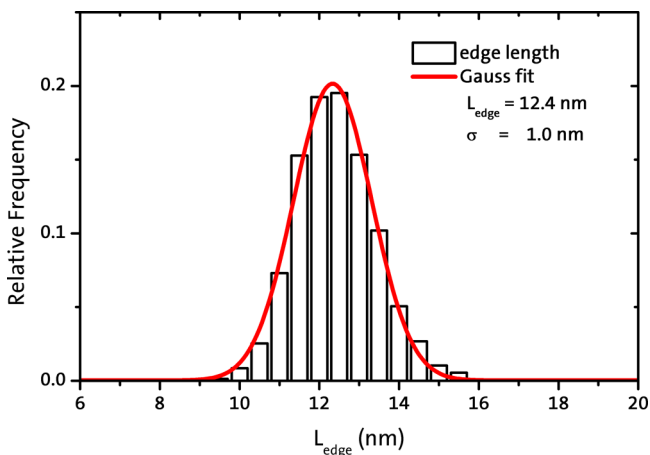


Figure 4. Size distribution of the cubic magnetite NPs as obtained from the minimal Feret diameters of Figure 3. The solid red curve depicts a normal distribution with an average edge length of $L_{\text{edge}} = 12.4$ nm and a standard deviation of $\sigma = 1.0$ nm.

gyration, $R_g = 6.4$ nm. The average edge length thus obtained, $L_{\text{edge}} = 2R_g = 12.8$ nm, is in reasonable agreement with the TEM result above. Although throughout this study we use the TEM value for the average edge length L_{edge} of the NPs, the use of the slightly larger SAXS value would not affect any of our conclusions.

The nanocubes were drop-cast into the nanofluidic containers as follows. First, we drop-casted 20 μL of a concentrated, 1.9 vol % dispersion (50 mg of $\text{Fe}_3\text{O}_4/\text{mL}$ of toluene) on top of the channel arrays. Once the solvent had slowly evaporated, we removed the excess NPs on top of the channels by gentle scraping using plastic tweezers and carried out SAXS/WAXS and SEM experiments.

Nanofluidic Containers. The nanofluidic containers consisted of specifically designed one-dimensional (1D) diffraction gratings. Each grating was made of 1750 parallel channels with a period of 200 nm, a depth of ~ 640 nm (~ 40 L), and an aspect ratio (channel depth/width) of approximately 5–10, distributed over a total area of 0.35×0.35 mm². The separation of the confining walls was systematically varied in the range of $70 \text{ nm} \leq W \leq 103$ nm, as determined by SEM. The channel walls were smooth and nearly parallel, thus facilitating confinement-induced assembly of the cubic NPs. For a cross-sectional SEM image of the gratings, see Figure 5.

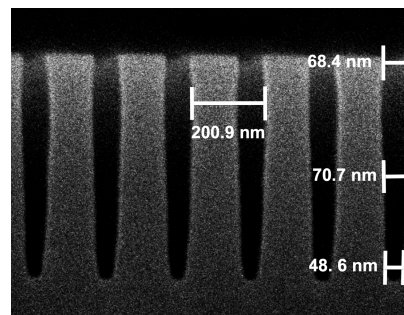


Figure 5. Cross-sectional SEM image of an empty nanofluidic container. In this particular case the wall separation is $W = 70$ nm.

Mesoscale Order in Reciprocal Space. The information in the SAXS data from the NP-filled nanofluidic containers are 2-fold. First, we observe a 1D diffraction pattern (horizontal line in the scattering pattern of Figure 1) due to the periodicity of the NP-filled nanofluidic container. In principle the diffraction pattern could be inverted to yield the average electron density profile across the channel, using either phase retrieval schemes^{33,34} or critical-dimension SAXS,³⁵ but the resolution is not sufficient for the small particles studied here. Second, owing to the thousand identical channels and hence the 1000-fold scattering volume compared to using a single channel for confinement, we are also sensitive to diffuse scattering.²⁸ In the present study, we used the diffuse SAXS data to probe both orientational and translational ordering of the anisotropic NPs.

In Figure 6 we show representative SAXS data collected from nanocubes drop-cast in nanofluidic containers. In panels (a) and (b) we present data obtained for wall separations $W = 94$ and 103 nm, respectively. In the former, incommensurate confinement ($W/L \approx 5.8$), there is more excess space available for the NPs, as compared to the latter commensurate case ($W/L \approx 6.4$), and we hence expect a lesser degree of NP order. For comparison, we also present SAXS data collected from a 1.9 vol

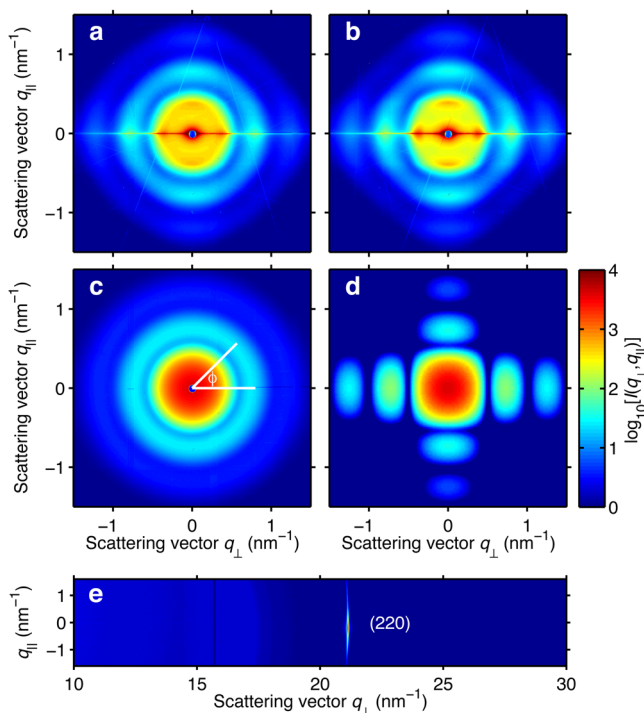


Figure 6. Anisotropic scattering pattern $I(q_{\perp}, q_{\parallel})$ obtained from cubic magnetite NPs in confinement, presented as a function of parallel (q_{\parallel}) and perpendicular (q_{\perp}) scattering vector components. SAXS data are presented for drop-cast NPs in nanofluidic channels with confining wall separations of (a) $W = 94$ nm ($W/L \approx 5.8$) and (b) $W = 103$ nm ($W/L \approx 6.4$). The horizontal line of enhanced intensity at $q_{\parallel} = 0$ is due to diffraction from the periodic array of nanofluidic channels, while the weak intensity streaks are Kossel lines originating from the silicon substrate.³⁶ (c) Isotropic SAXS pattern obtained from a bulk NP dispersion (NP volume fraction 1.9%). The white lines depict the azimuthal angle $\phi = \arctan(q_{\parallel}/q_{\perp})$. (d) Model SAXS pattern from individual cubic NPs, which exhibit rotational symmetry in the plane parallel to the confining walls. (e) WAXS data for $W = 103$ nm, showing the (220) reflection of magnetite. The black vertical line at $q_{\perp} \approx 16$ nm⁻¹ is due to the dead area between detector modules. All data are shown on a logarithmic intensity scale, and the SAXS data have been mutually normalized.

% bulk dispersion of the nanocubes in panel (c). The effect of confinement on the SAXS pattern is striking; whereas the disordered bulk dispersion exhibits an isotropic scattering pattern, spatial confinement induces both orientational and translational order of the cubic NPs, most strongly manifested as 2-fold symmetry in the SAXS pattern and as pronounced peaks at $(q_{\perp}, q_{\parallel}) \approx (0, \pm 0.4)$ nm⁻¹. These data provide the first direct and unambiguous experimental evidence that spatial confinement induces the ordering of cubic NPs.

The SAXS pattern from NP ensembles depends on both the particles' shape (form factor) and interparticle correlations (structure factor), and for anisotropic particles these are difficult to disentangle. In order to obtain further insight into the above SAXS data, we present in Figure 6(d) the scattering pattern based on a simple model calculation from dilute monodisperse NPs, i.e., a form factor. Our confining wells impose constraints on NP rotations in the azimuthal direction but not in the direction perpendicular to the walls (q_{\perp}). In the model we therefore assume that one face of each individual cubic NP orients parallel to the confining walls but that the NPs

can rotate randomly around the q_{\perp} axis. By averaging the SAXS pattern of a nanocube over possible orientations we obtain

$$\langle I(q_{\perp}, q_{\parallel}) \rangle = C \operatorname{sinc}^2(q_{\perp}D) \int_0^{2\pi} \operatorname{sinc}^2(q_{\parallel}D \sin \alpha) \operatorname{sinc}^2(q_{\parallel}D \cos \alpha) d\alpha \quad (1)$$

where α is the angle of rotation, $D = L/2$, and C is a normalization constant. Although a quantitative agreement between experimental data and the model would require us to include the true shape and polydispersity of the nanocubes (Figures 3 and 4) as well as particle–particle correlations,^{37–39} our simple model SAXS pattern reproduces several features of the experimental data. Most importantly, we observe 2-fold symmetry in the SAXS pattern, with the NP rotations resulting in stronger higher-order peaks in the perpendicular (q_{\perp}) compared to the parallel (q_{\parallel}) direction, in agreement with the experimental data. However, the experimental data also exhibit important features which are not contained in the simple model calculation. First, the degree of azimuthal order depends on the wall separation W , as observed from the more pronounced anisotropy in the data in Figure 6(b) compared to that in 6(a). Second, the peaks at $(q_{\perp}, q_{\parallel}) \approx (0, \pm 0.4)$ nm⁻¹, which are due to correlations between particles in the parallel direction, are stronger in Figure 6(b) than in Figure 6(a). We will return to these features at a later stage.

The cubic magnetite NPs are crystalline, with their facets terminated on the $\{100\}$ planes.²⁶ The confinement-induced ordering of one NP face parallel to the slit walls thus also implies the alignment of the corresponding crystalline $\langle 100 \rangle$ direction. This is indeed the case as observed from the WAXS data in Figure 6(e), where a narrow (220) reflection of magnetite is present in the perpendicular direction q_{\perp} , in stark contrast to a uniform diffraction ring caused by disordered NPs. Importantly, the narrow distribution of parallel scattering vector components q_{\parallel} shows that one face of the cubic NPs aligns parallel to the confining walls.

Having qualitatively verified that spatial confinement induces the ordering of cubic NPs, we next turn to quantifying the effect. For this purpose, we start by plotting in Figure 7(a) the aforementioned 2-fold symmetry of Figure 6 in terms of the SAXS intensity $I(Q, \phi)$, determined at the fixed scattering vector length $Q = \sqrt{q_{\parallel}^2 + q_{\perp}^2} = 0.8$ nm⁻¹, i.e., at the second maximum, as a function of azimuthal angle $\phi = \arctan(q_{\parallel}/q_{\perp})$. (See Figure 6(c) for a graphical definition.) The data obtained from the confined nanocubes exhibit two important features. First, we observe a 2-fold symmetry in both cases, as inferred already from Figure 6. Second, the azimuthal order is found to be enhanced for commensurate ($W = 103$ nm) compared to incommensurate confinement ($W = 94$ nm). In order to quantify the latter effect, we present in Figure 7(b) WAXS data obtained for a scattering vector magnitude corresponding to the (220) reflection, again collected as a function of the azimuthal angle ϕ . We note that the small offset of the (220) reflection from $\phi = 0$ is due to a minor misalignment of the diffraction grating with respect to the detector. In line with the data in panel (a), commensurate confinement ($W = 103$ nm) leads to a narrower distribution of azimuthal angles ϕ compared to the incommensurate wall separation ($W = 94$ nm); in the particular cases of Figure 7(b), we obtain full width at half maxima of $\sim 1.3^\circ$ and 2.5° , respectively. These data imply that the wall separation W can indeed be used to control the orientational ordering of cubic NPs.

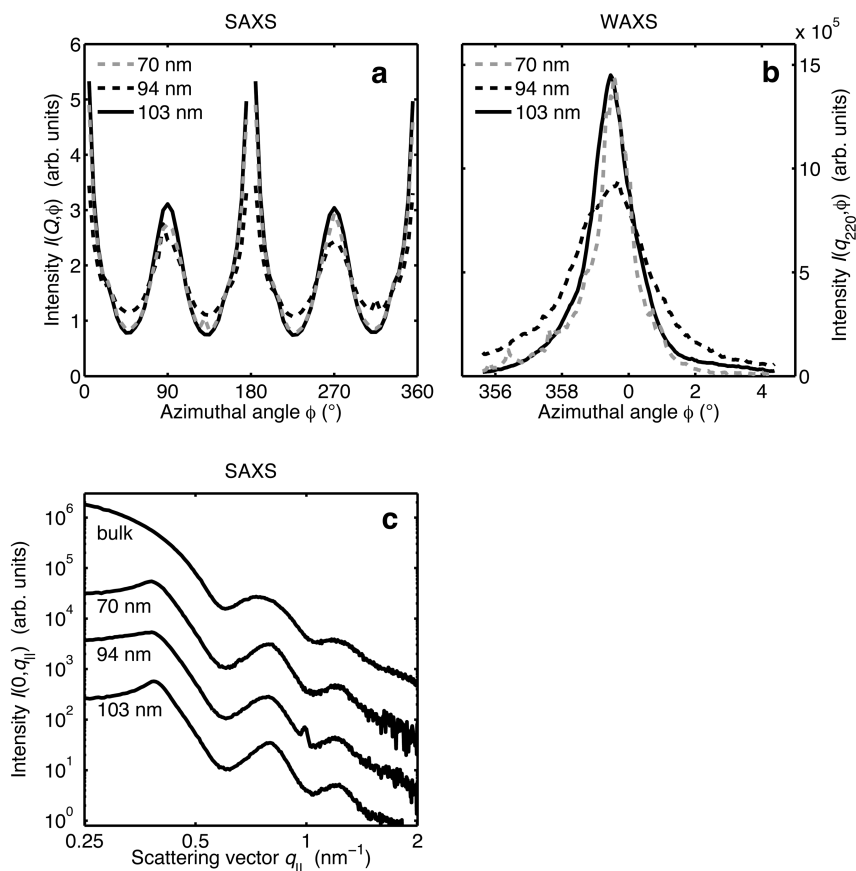


Figure 7. Scattering data obtained from cubic NPs drop-cast in either incommensurate ($W = 94$ nm, $W/L \approx 5.8$) or commensurate ($W = 103$ nm, $W/L \approx 6.4$; $W = 70$ nm, $W/L \approx 4.3$) nanofluidic containers, as obtained from Figure 6. (a) Experimental SAXS intensities $I(Q, \phi)$ monitored at the fixed scattering vector length $Q = 0.8$ nm $^{-1}$ as a function of azimuthal angle $\phi = \arctan(q_{||}/q_{\perp})$. We have disregarded data around $q_{||} = 0$ (corresponding to $\phi = 0$ and 180°) due to diffraction from the grating. (b) WAXS intensities $I(q_{220}, \phi)$ of the (220) reflection, collected as a function of azimuthal angle ϕ . (c) Parallel cut of SAXS intensity $I(q_{\perp}, q_{||})$ at $q_{\perp} = 0$, i.e., $I(0, q_{||})$. The corresponding bulk data are shown for comparison, and the curves are vertically offset for clarity. The small peak at $q_{||} \approx 1$ nm $^{-1}$ for $W = 94$ nm is due to a Kossel line.³⁶

Let us next return to the translational order of the cubic NPs. In order to facilitate the discussion, we present in Figure 7(c) parallel cuts $I(0, q_{||})$ of the experimental data shown in Figure 6(a)–(c), i.e., $I(q_{\perp}, q_{||})$ for $q_{\perp} = 0$. The translational ordering of the cubic NPs parallel to the confining walls is manifested as the intensity peak at $q_{||} \approx 0.4$ nm $^{-1}$ in the scattering intensity. Again, the intensity peak is more pronounced for $W = 103$ than for 94 nm, demonstrating a more developed parallel translational NP order in commensurate confinement. We further note that the peak position for commensurate confinement, $q_{||}^{\max} = 0.385$ nm $^{-1}$, implies the smallest possible distance between NP centers, $2\pi/q_{||}^{\max} \approx 16.3$ nm, and hence that neighboring NPs order face to face. These data evidence that the wall separation W also governs the translational ordering of cubic NPs.

We have verified the high degree of order for the wall separation $W = 70$ nm ($W/L \approx 4.3$) in Figure 7, providing further support for the hypothesis that commensurate confinement induces pronounced NP ordering. This observation is readily rationalized in terms of space available for the cubic NPs. In the case of commensurate confinement, an integer multiple times the edge length barely fits in the confining slit, whereby excluded volume effects hinder azimuthal rotations of the NPs and lead to pronounced translational ordering. For incommensurate confinement, in turn, more space is available

for azimuthal NP rotations, resulting in a less pronounced translational order.

Mesoscale Order in Real Space. So far we have discussed the mesoscale order as determined by X-ray scattering, which provides volume-averaged reciprocal-space information on confinement-induced NP ordering. In order to complement these data in real space, we present SEM images of cross sections from cleaved, NP-filled gratings in Figure 8 for the same confining channel widths as above: (a) $W = 94$ and (b) 103 nm. The SEM data verify our main conclusions based on SAXS. First, spatial confinement induces the ordering of the cubic NPs, resulting in five and six particle layers across the confining slit for $W/L \approx 5.8$ and 6.4 , respectively. This observation is further highlighted in the green insets, showing checkerboard-like Fourier-filtered transforms of the SEM image. Second, the degree of order depends on the wall separation W . This is clearly seen in the green dashed frame, where we observe six well-defined layers of NPs aligned parallel to the confining surfaces, as expected for $W/L \approx 6.4$.

Drying-mediated assembly is a subtle phenomenon, which may raise questions about reproducibility in the confinement-induced assembly demonstrated here. The SEM images of Figure 8, which represent single realizations of assembly in confinement, do indeed exhibit minor deviations between different channels. It should be realized, however, that the SAXS and WAXS experiments have been carried out on a

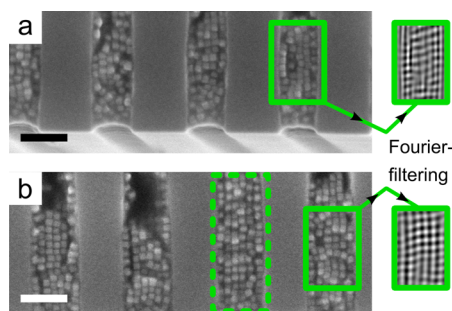


Figure 8. Cross-sectional SEM images of cubic magnetite NPs drop-cast in nanofluidic containers. (a) The incommensurate wall separation $W = 94$ nm ($W/L \approx 5.8$) leads to less-ordered NP assemblies while (b) the commensurate wall separation $W = 103$ nm ($W/L \approx 6.4$) results in more pronounced NP ordering. The insets show Fourier-filtered transforms of part of the NP-filled confining slit, while the dashed frame highlights the ordering of the NPs. Scale bars: 100 nm.

thousand different confining channels simultaneously for each wall separation W .

CONCLUSIONS

By combining SAXS, WAXS, and SEM experiments on cubic magnetite NPs drop-cast in nanofluidic containers, we have demonstrated that spatial confinement can be employed to induce their mesoscale assembly. We have further shown that the cubic NPs align one of their faces, and hence the corresponding $\{100\}$ planes, parallel to the confining slit walls. The confinement-induced assembly of anisotropic NPs, as demonstrated here, provides a promising route toward nanoscale devices with tunable anisotropic properties.

Finally, we comment briefly on the possibility of further refining the confinement-induced mesoscale order of cubic NPs as demonstrated here. First, we note that the wall separation W becomes narrower in the bottom part of the confining channel (Figure 5), resulting in modified packing constraints for the NPs. For the NP-filled containers we also observe defects, i.e., regions void of NPs, in the channels (Figure 8). A future improvement could thus be to use nanofluidic containers consisting of channels with essentially parallel walls as in ref 33, although manufacturing such channels of sufficient depth and with a wall separation in the range of $50 \text{ nm} \leq W \leq 100 \text{ nm}$ is highly challenging. Second, we have focused on only one type of NP and nanofluidic container, and it is probable that the degree of NP order could be improved by modifying the particle–wall interactions. Indeed, work on confined spherical particles has indicated that the formation of dense particle monolayers at the confining walls enhances ordering throughout the slit.⁴⁰ However, the NP ordering results from a subtle interplay between energetics and entropy, and a proper analysis of how particle–particle and particle–wall attractions affect the NP ordering must include all of these effects. It is our hope that the experimental results presented here stimulate interest in simulations on NP assembly in confinement.

AUTHOR INFORMATION

Corresponding Authors

*E-mail: lennart.bergstrom@mmk.su.se.

*E-mail: kim.nygard@chem.gu.se.

Notes

The authors declare no competing financial interest.

ACKNOWLEDGMENTS

We acknowledge financial support from the European Commission under the Seventh Framework Program by means of the grant agreement for the Integrated Infrastructure Initiative no. 262348, European Soft Matter Infrastructure (ESMI). M.A. and L.B. acknowledge financial support from the Swedish Research Council and the Knut and Alice Wallenberg Foundation through project 3DEM-NATUR. Finally, K.N. thanks the Swedish Research Council for support.

REFERENCES

- Ozin, G. A.; Hou, K.; Lotsch, B. V.; Cademartiri, L.; Puzzo, D. P.; Scotognella, F.; Ghadimi, A.; Thomson, J. Nanofabrication by self-assembly. *Mater. Today* **2009**, *11*, 12–23.
- Nie, Z.; Petukhova, A.; Kumacheva, E. Properties and emerging applications of self-assembled structures made from inorganic nanoparticles. *Nat. Nanotechnol.* **2010**, *5*, 15–25.
- Li, F.; Josephson, D. P.; Stein, A. Colloidal assembly: the road from particles to colloidal molecules and crystals. *Angew. Chem., Int. Ed.* **2011**, *50*, 360–388.
- Han, W.; Lin, Z. Learning from “coffee rings”: ordered structures enabled by controlled evaporative self-assembly. *Angew. Chem., Int. Ed.* **2012**, *51*, 1534–1546.
- Wang, Y.; Kanjanboos, P.; McBride, S. P.; Barry, E.; Lin, X.-M.; Jaeger, H. M. Mechanical properties of self-assembled nanoparticle membranes: stretching and bending. *Faraday Discuss.* **2015**, *181*, 325–338.
- Glotzer, S. C.; Solomon, M. J. Anisotropy of building blocks and their assembly into complex structures. *Nat. Mater.* **2007**, *6*, 557–562.
- Ye, X.; Millan, J. A.; Engel, M.; Chen, J.; Diroll, B. T.; Glotzer, S. A.; Murray, C. B. Shape alloys of nanorods and nanospheres from self-assembly. *Nano Lett.* **2013**, *13*, 4980–4988.
- Grzelczak, M.; Vermant, J.; Furst, E. M.; Liz-Marzán, L. M. Directed self-assembly of nanoparticles. *ACS Nano* **2010**, *4*, 3591–3605.
- Singamaneni, S.; Bliznyuk, V. N.; Binek, C.; Tsybmal, E. Y. Magnetic nanoparticles: recent advances in synthesis, self-assembly and application. *J. Mater. Chem.* **2011**, *21*, 16819–16845.
- Singh, G.; Chan, H.; Baskin, A.; Gelman, E.; Král, P.; Klajn, R. Self-assembly of magnetite nanocubes into helical superstructures. *Science* **2014**, *345*, 1149–1153.
- Singh, G.; Chan, H.; Udayabhaskararao, T.; Gelman, E.; Peddis, D.; Baskin, A.; Leitus, G.; Král, P.; Klajn, R. Magnetic field-induced self-assembly of iron oxide nanocubes. *Faraday Discuss.* **2015**, *181*, 403–421.
- Hoffelner, D.; Kundt, M.; Schmidt, A. M.; Kentzinder, E.; Bender, P.; Disch, S. Directing the orientational alignment of anisotropic magnetic nanoparticles using dynamic magnetic fields. *Faraday Discuss.* **2015**, *181*, 449–461.
- Dai, Q.; Rettner, C. T.; Davis, B.; Cheng, J.; Nelson, A. Topographically directed self-assembly of goldnanoparticles. *J. Mater. Chem.* **2011**, *21*, 16863–16865.
- Ferraro, M. E.; Bonnecaze, R. T.; Truskett, T. M. Graphoepitaxy for pattern multiplication of nanoparticle monolayers. *Phys. Rev. Lett.* **2014**, *113*, 085503.
- Tebbe, M.; et al. Optically anisotropic substrates via wrinkle-assisted convective assembly of gold nanorods on macroscopic areas. *Faraday Discuss.* **2015**, *181*, 243–260.
- Jones, M. R.; Macfarlane, R. J.; Lee, B.; Zhang, J.; Young, K. L.; Senesi, A. J.; Mirkin, C. A. DNA-nanoparticle superlattices formed from anisotropic building blocks. *Nat. Mater.* **2010**, *9*, 913–917.
- Lu, F.; Yager, K. G.; Zhang, Y.; Xin, H.; Gang, O. Superlattices assembled through shape-induced directional binding. *Nat. Commun.* **2015**, *6*, 6912.
- Fortini, A.; Dijkstra, M. Phase behaviour of hard spheres confined between parallel hard plates: manipulation of colloidal crystal

structures by confinement. *J. Phys.: Condens. Matter* **2006**, *18*, L371–L378.

(19) Liu, G.; Ramírez-Hernández, A.; Yoshida, H.; Nygård, K.; Satapathy, D. K.; Bunk, O.; de Pablo, J. J.; Nealey, P. F. Morphology of lamellae-forming block copolymer films between two orthogonal chemically nanopatterned striped surfaces. *Phys. Rev. Lett.* **2012**, *108*, 065502.

(20) Bates, C. M.; Seshimo, T.; Maher, M. J.; Durand, W. J.; Cushen, J. D.; Dean, L. M.; Blachut, G.; Ellison, C. J.; Wilson, C. G. Polarity-switching top coats enable orientation of sub-10-nm block copolymer domains. *Science* **2012**, *338*, 775–779.

(21) Pieranski, P.; Strzelecki, L.; Pansu, B. Thin colloidal crystals. *Phys. Rev. Lett.* **1983**, *50*, 900–903.

(22) Nesper, S.; Bechinger, C.; Leiderer, P.; Palberg, T. Finite-size effects on the closest packing of hard spheres. *Phys. Rev. Lett.* **1997**, *79*, 2348–2351.

(23) Oğuz, E. C.; Marechal, M.; Ramiro-Manzano, F.; Rodriguez, L.; Messina, R.; Meseguer, F. J.; Löwen, H. Packing confined hard spheres denser with adaptive prism phases. *Phys. Rev. Lett.* **2012**, *109*, 218301.

(24) Renaud, G.; Lazzari, R.; Leroy, F. Probing surface and interface morphology with grazing incidence small angle X-ray scattering. *Surf. Sci. Rep.* **2009**, *64*, 255–380.

(25) Jiang, Z.; Lin, X.-M.; Sprung, M.; Narayanan, S.; Wang, J. Capturing the crystalline phase of two-dimensional nanocrystal superlattices in action. *Nano Lett.* **2010**, *10*, 799–803.

(26) Disch, S.; Wetterskog, E.; Hermann, R. P.; Salazar-Alvarez, G.; Busch, P.; Brückel, T.; Bergström, L.; Kamali, S. Shape induced symmetry in self-assembled mesocrystals of iron oxide nanocubes. *Nano Lett.* **2011**, *11*, 1651–1656.

(27) Goodfellow, B. W.; Yu, Y.; Bosov, C. A.; Smilgies, D.-M.; Korgel, B. A. The role of ligand packing frustration in body-centered cubic (bcc) superlattices of colloidal nanocrystals. *J. Phys. Chem. Lett.* **2015**, *6*, 2406–2412.

(28) Nygård, K.; Kjellander, R.; Sarman, S.; Chodankar, S.; Perret, E.; Buitenhuis, J.; van der Veen, J. F. Anisotropic pair correlations and structure factors of confined hard-sphere fluids: an experimental and theoretical study. *Phys. Rev. Lett.* **2012**, *108*, 037802.

(29) Wetterskog, E.; Agthe, M.; Mayence, A.; Grins, J.; Wang, D.; Rana, S.; Ahniyaz, A.; Salazar-Alvarez, G.; Bergström, L. Precise control over shape and size of iron oxide nanocrystals suitable for assembly into ordered particle arrays. *Sci. Technol. Adv. Mater.* **2014**, *15*, 055010.

(30) Wetterskog, E.; Tai, C.-W.; Grins, J.; Bergström, L.; Salazar-Alvarez, G. Anomalous magnetic properties of nanoparticles arising from defect structures: topotaxial oxidation of $\text{Fe}_{1-x}\text{O}/\text{Fe}_{3-\delta}\text{O}_4$ core shell nanocubes to single-phase particles. *ACS Nano* **2013**, *7*, 7132–7144.

(31) Kraft, P.; et al. Performance of single-photon-counting PILATUS detector modules. *J. Synchrotron Radiat.* **2009**, *16*, 368–375.

(32) Lutterotti, L. Total pattern fitting for the combined size-strain-stress-texture determination in thin film diffraction. *Nucl. Instrum. Methods Phys. Res., Sect. B* **2010**, *268*, 334–340.

(33) Nygård, K.; Satapathy, D. K.; Bunk, O.; Perret, E.; Buitenhuis, J.; David, C.; van der Veen, J. F. Grating-based holographic X-ray diffraction: theory and application to confined fluids. *J. Appl. Crystallogr.* **2009**, *42*, 1129–1138.

(34) Bunk, O.; Diaz, A.; Pfeiffer, F.; David, C.; Schmitt, B.; Satapathy, D. K.; van der Veen, J. F. Diffractive imaging for periodic samples: retrieving one-dimensional concentration profiles across microfluidic channels. *Acta Crystallogr., Sect. A: Found. Crystallogr.* **2007**, *63*, 306–314.

(35) Jones, R. L.; Hu, T.; Soles, C. L.; Lin, E. K.; Reano, R. M.; Pang, S. W.; Casa, D. M. Real-time shape evolution of nanoimprinted polymer structures during thermal annealing. *Nano Lett.* **2006**, *6*, 1723–1728.

(36) Morris, W. G. Crystal orientation and lattice parameters from Kossel lines. *J. Appl. Phys.* **1968**, *39*, 1813–1823.

(37) Förster, S.; Timmann, A.; Konrad, M.; Schellbach, C.; Meyer, A.; Funari, S. S.; Mulvaney, P.; Knott, R. Scattering curves of ordered mesoscopic materials. *J. Phys. Chem. B* **2005**, *109*, 1347–1360.

(38) Yager, K. G.; Zhang, Y.; Lu, F.; Gang, O. Periodic lattices of arbitrary nano-objects: modeling and applications for self-assembled systems. *J. Appl. Crystallogr.* **2014**, *47*, 118–129.

(39) Senesi, A. J.; Lee, B. Small-angle scattering of particle assemblies. *J. Appl. Crystallogr.* **2015**, *48*, 1172–1182.

(40) Satapathy, D. K.; Bunk, O.; Jefimovs, K.; Nygård, K.; Guo, H.; Diaz, A.; Perret, E.; Pfeiffer, F.; David, C.; Wegdam, G. H.; van der Veen, J. F. Colloidal monolayer trapped near a charged wall: a synchrotron x-ray diffraction study. *Phys. Rev. Lett.* **2008**, *101*, 136103.